

# Optical Funnel to Guide and Focus Virus Particles for X-Ray Diffractive Imaging

Salah Awel<sup>1,2</sup>, Sebastian Lavin-Varela,<sup>3</sup> Nils Roth,<sup>1,4</sup> Daniel A. Horke<sup>1,5</sup>, Andrei V. Rode<sup>1,3,\*</sup>,  
Richard A. Kirian,<sup>6</sup> Jochen Küpper,<sup>1,2,4</sup> and Henry N. Chapman<sup>1,2,4</sup>

<sup>1</sup>Center for Free-Electron Laser Science, Deutsches Elektronen-Synchrotron (DESY), Notkestrasse 85, Hamburg 22607, Germany


<sup>2</sup>Center for Ultrafast Imaging, Universität Hamburg, Luruper Chaussee 149, Hamburg 22761, Germany

<sup>3</sup>Laser Physics Centre, Research School of Physics, Australian National University, Canberra ACT 2601, Australia

<sup>4</sup>Department of Physics, Universität Hamburg, Luruper Chaussee 149, Hamburg 22761, Germany

<sup>5</sup>Radboud University, Institute for Molecules and Materials, Heyendaalseweg 135, Nijmegen 6525 AJ, Netherlands

<sup>6</sup>Department of Physics, Arizona State University, Tempe, Arizona 85287, USA

 (Received 14 January 2022; revised 17 March 2022; accepted 22 March 2022; published 22 April 2022)

Photophoretic forces are induced when light causes a net momentum exchange between a particle and a surrounding gas. Such forces have been shown to be a robust means for trapping and guiding particles in air over long distances. Here, we apply the concept of an optical funnel for the delivery of bioparticles to the focus of an x-ray free-electron laser (XFEL) for femtosecond x-ray diffractive imaging. We provide the experimental demonstration of transversely compressing a high-speed beam of aerosolized viruses via photophoretic forces in a low-pressure gas environment. Relative temperature gradients induced on the viruses by the laser are estimated via particle-velocimetry measurements. The results demonstrate the potential for an optical funnel to improve particle-delivery efficiency in XFEL imaging and spectroscopy.

DOI: [10.1103/PhysRevApplied.17.044044](https://doi.org/10.1103/PhysRevApplied.17.044044)

## I. INTRODUCTION

X-ray free-electron laser (XFEL) facilities have the potential to enable atomic resolution images of biomolecules at physiological temperatures and with time resolution in the femtosecond regime [1,2]. Since 2009, the serial femtosecond crystallography (SFX) method has yielded nearly 500 protein-structure entries in the protein data bank, many of which are from dynamic systems and are time sequenced with time steps down to 100 fs [3–5]. Single-particle imaging (SPI) aims to extend XFEL imaging to include isolated noncrystallized biomolecules, which would allow the observation of functional molecular motions that may otherwise be hindered in the crystal environment. With the high data-collection rates possible at XFEL facilities [6] combined with the rapid shock-freeze method [7], SPI might enable the detection of rare intermediate states.

The most significant present-day challenge in SPI is the production of high-density nanoparticle beams that can be directed to an x-ray beam of diameter 100–1000 nm in a low-pressure environment [8–12]. Nearly all SPI experiments have utilized aerodynamic focusing injectors for particle delivery [13–15]. Such injectors are well developed and can generate particle beams with diameters on

the order of 10  $\mu\text{m}$  [10,12,16,17] but the fraction of x-ray pulses that intercept a biomolecule still remains at less than 0.1 %, for a 100-nm x-ray focus. At this rate, roughly one day of continuous data collection at a 10-kHz detector frame rate would be needed for a full atomic resolution data set consisting of approximately  $10^6$  diffraction patterns. For these reasons, we consider optical forces as a means to increase the target precision and density of SPI injection systems [18–22].

Previously, we have proposed and investigated an “optical funnel” that uses a focused hollow-core optical vortex beam to guide particles into a tight focus [23,24]. Our design utilizes a laser that counterpropagates against the particle beam to increase the particle density both by slowing the particles as well as by forcing them closer to the beam axis. The inclusion of a surrounding gas activates photophoretic forces, caused by light absorption and subsequent momentum exchange with gas molecules. Photophoretic forces may be larger than optical scattering or gradient forces by orders of magnitude [19,24,25]. The effectiveness of this optical-funnel scheme is complicated by a number of factors, including the optical and thermal properties of the particles, heating and radiation damage, x-ray scattering background caused by the gas, and the three-dimensional profile of the optical beam. While many questions remain, the basic feasibility of the optical-funnel concept has been supported by our preliminary simulation and experimental study, in which photophoretic

\*avr111@physics.anu.edu.au

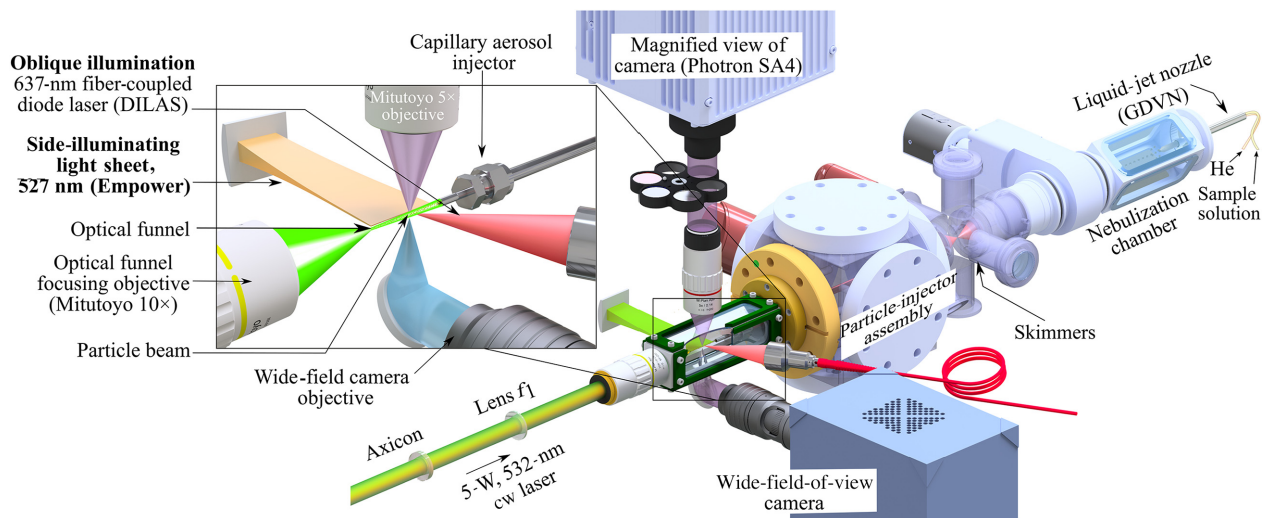


FIG. 1. The basic experimental setup for aerosol particle-beam imaging and focusing.

forces have been directly measured by counterbalancing microparticles against the gravitational force [23,24,26]. Our previous efforts to demonstrate an optical funnel on high-speed particle beams have yielded clear evidence of strong photophoretic forces but no evidence of particle-beam compression, which may have been due to the rapid divergence of the optical beam and limited laser-particle interaction length.

In this paper, we demonstrate particle-beam compression with an optical funnel constructed from a low-divergence hollow-core first-order Bessel beam that extends the particle-laser interaction length by a factor of up to 1000 as compared with a Gaussian beam. The basic experimental setup, shown in Fig. 1, consists of assemblies for optical-funnel beam shaping, aerosolized-particle-beam formation, and high-speed optical imaging.

## II. OPTICAL FUNNEL

The optical-funnel profile is achieved by forming a first-order quasi-Bessel beam with a spiral phase plate and an axicon lens and then reimaging the beam inside the chamber with a demagnifying collimator [24,27,28]. The resulting beam changes its size due to the continuously changing magnification along the propagation direction ( $z$  axis), as shown in Fig. 2. Since optimization of the optical-funnel geometry for guiding a particular stream of particles is a multiparameter task, we carry out simulations based on Fourier optics [29], modifying the results of Brzobohaty et al. [30] and verifying the results using analytical expressions [31], as discussed in detail in the Supplemental Material [32], Sec. S-I. Figure 2 shows a comparison of the experimental laser-beam profiles along with the numerical simulations [33]. For this comparison, we form an optical funnel with a 532-nm cw Gaussian beam with an output

waist  $w_0 = 1.4$  mm, which is converted to a first-order Laguerre-Gaussian vortex beam with topological charge  $l = 1$  using a 16-step phase plate. The Bessel beam is formed using an axicon with a wedge angle  $\alpha_0 = 0.5^\circ$ . The beam is reimaged by a demagnifying collimator with  $f_1 = 200$  mm and  $f_2 = 20$  mm. The formation of this beam is illustrated in Fig. S1 in the Supplemental Material [32]. The resulting optical funnel has a minimum peak-to-peak diameter of  $7.5 \mu\text{m}$  and an angle of divergence in the first bright ring of approximately  $1.3 \times 10^{-3}$  rad.

We direct this optical funnel into a small chamber where we prepare a counterpropagating particle beam in a low-pressure (0.4–0.9 mbar) helium gas environment as shown in Fig. 1. Samples of  $265 \times 265 \times 445 \text{ nm}^3$  *Cydia pomonella* granulovirus capsid particles [34] or  $2 \mu\text{m}$  fluorescent polystyrene spheres are aerosolized with a gas-dynamic virtual nozzle [35,36] at approximately atmospheric pressure and subsequently drawn through a gas nozzle and/or skimmer stage [16,37,38] in order to control the gas pressure. A collimated beam of particles is ejected from a 2-mm-inner-diameter capillary. The particles have speeds in the range of 2–20 m/s, depending on the gas differential pressures. The particle-laser interactions are observed by pulsed-laser Rayleigh-scattering imaging, which localizes the coordinates of individual particles [11,12,16].

## III. PARTICLE-BEAM COMPRESSION

### A. Particle trajectories

Figure 3(a) shows raw Rayleigh-scattering images of granulovirus particles exposed to a 0.5-W optical funnel at 0.99-mbar pressure. The particles are illuminated by 637-nm 100-ns laser flashes repeating at 25 kHz and

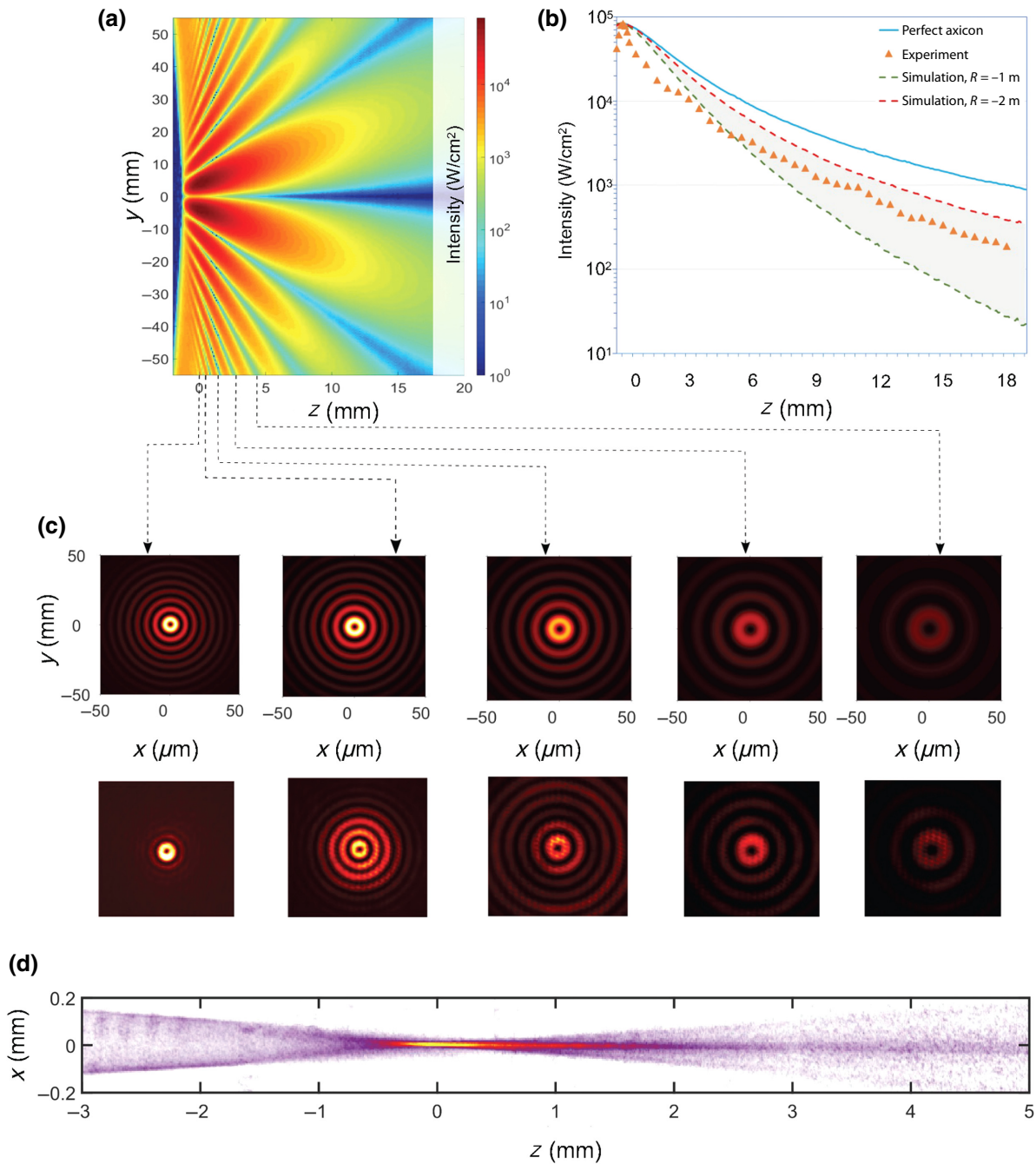


FIG. 2. The slow-diverging optical funnel formed by demagnifying a quasi-Bessel beam with a Keplerian collimator. (a) The simulated optical funnel: the distances are from the maximum-intensity position. (b) A comparison between the experimental intensity profile and a calculated profile in the first ring of the funnel at a total laser power of 1 W. The solid line describes a perfect axicon, whereas the shaded area between the dashed lines indicates the intensity profiles for imperfect axicons with a radius of curvature within the range from 1 m to 2 m of the front face on the axicon. (c) Beam profiles at various cross sections of the optical funnel: the top row shows simulation results, while the bottom row displays the measured profiles. (d) The optical-funnel profile generated by time integrating air scattering in the beam path. The laser beam propagates from left to right toward the particle nozzle.

the scattered light is imaged by a camera. Stroboscopic exposures of the same particle appear in one camera frame, which allows us to calculate the velocities and accelerations from the particle centroid positions [39], as

shown in Figs. 3(b)–3(e). The optical beam propagates in the  $+z$  direction. Based on the observed accelerations of  $2 - 10 \times 10^3 \text{ m/s}^2$  in Figs. 3(b)–3(e), along with an estimated granulovirus mass of  $2.2 \times 10^{-14} \text{ g}$  calculated

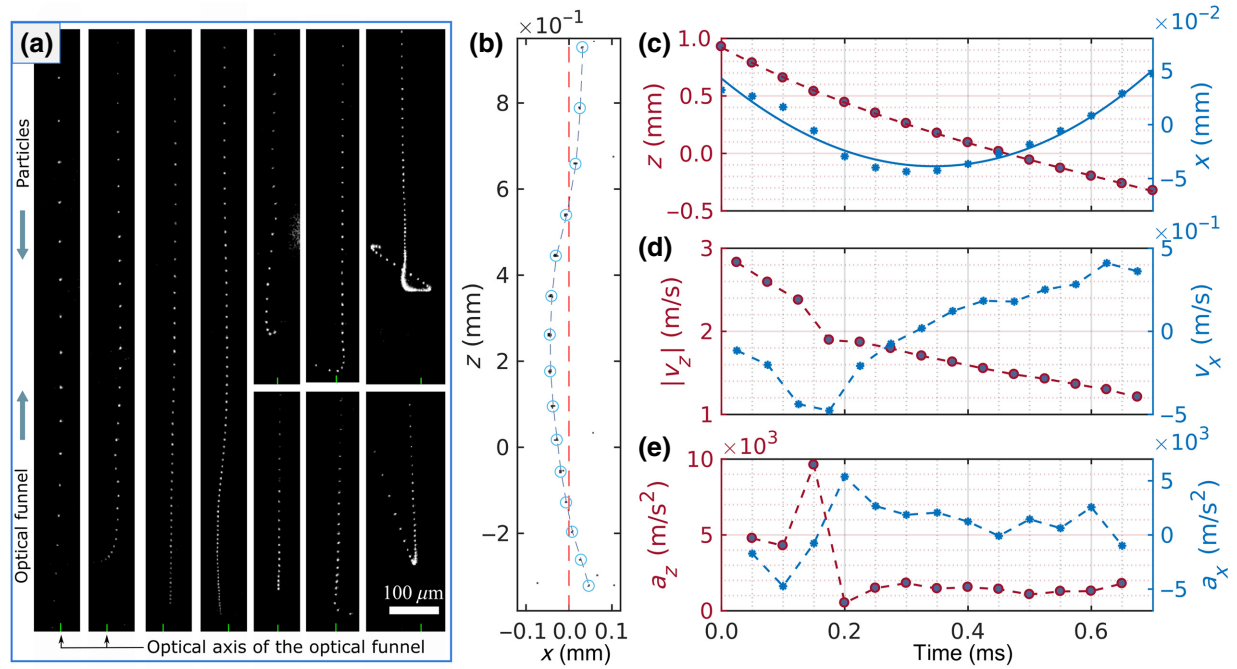


FIG. 3. Granulovirus trajectories recorded with 25-kHz illumination and 0.99-mbar chamber gas pressure. (a) Background-corrected raw images showing particle trajectories in a 2.0-W optical funnel. (b) Centroid positions of a single granulovirus particle trajectory in a 0.5-W optical funnel. The optical axis of the optical funnel is indicated by the dashed red line. (c) Calculated  $x$  (blue) and  $z$  (red) positions, velocities, and accelerations based on particle centroids in (b).

from the GV density  $1.4 \text{ g/cm}^3$  [40], we estimate forces of 0.044–0.22 pN. Particle trajectories in which the viruses dramatically change direction [as seen in Fig. 3(a)] are never observed in the absence of the optical funnel.

Figure 4(a) shows particle-density maps formed from Rayleigh-scattering images with 527-nm-illumination laser flashes reduced to 1 kHz to avoid overlapping particle images. Figure 4(a) shows the effect of a 0.5-W optical funnel on the granulovirus particle beam at 0.4 mbar pressure. The top and bottom density maps compare the densities when the laser is off and on, respectively, while Fig. 4(b) shows plots of the transverse profiles of the particle beams averaged over the  $z = 0.5 \pm 0.1 \text{ mm}$  region. Lorentzian fits to these profiles show that the optical funnel induces an approximately threefold increase in peak particle density, while the particle-beam full width at half maximum (FWHM) reduces by a factor of 2. Figure 4(c) shows density maps of 2- $\mu\text{m}$ -diameter polystyrene particle beams at 0.5 mbar chamber pressure, at laser powers of 0 W, 2.5 W, and 5.0 W. The focus of the optical funnel is located at the position  $x = z = 0$ , outside the field of view of the images. The radial profiles of the particle beams, averaged over  $z = [2.4, 2.6] \text{ mm}$ , are plotted in Fig. 4(d). The Lorentzian fits show that the optical funnel causes the peak particle densities to increase by factors of approximately 3 and 5 for 2.5 W and 5 W laser powers, respectively. Further

details on the measurement conditions are listed in Fig. S4 and Table S1 in the Supplementary Material [32].

In our observations, laser powers of 0.5 W and above result in obvious changes to the particle trajectories. The particle-beam compression effect does not confine the particles to the dark 7.5- $\mu\text{m}$  core of the optical funnel as desired; the particle-beam density increases within a broader approximately 150- $\mu\text{m}$ -diameter region, which may be due to the similarly broad initial beam. This could be improved by better matching the phase-space emittance of the particle beam and the acceptance of the optical funnel [7,17]. Along with the transverse compression effect, we also observe increases in the particle-beam density at progressively larger  $z$  values (closer to the nozzle) as the laser power is increased. Figure 5 shows the transverse ( $x$ ) profiles of polystyrene particle-beam densities at  $z = 5.5 \text{ mm}$  from the optical-funnel focus for five different laser powers, along with corresponding profiles for a range of  $z$  values between 5.2 mm and 7.2 mm. The observed  $z$  dependence of the particle density suggests that significant particle-laser interactions begin before particles reach the laser focus. As the particles slow down, they interact with the laser beam for longer durations and with sufficient laser power the particles begin to stop completely and reverse direction, as shown in Fig. S4 in the Supplemental Material [32].

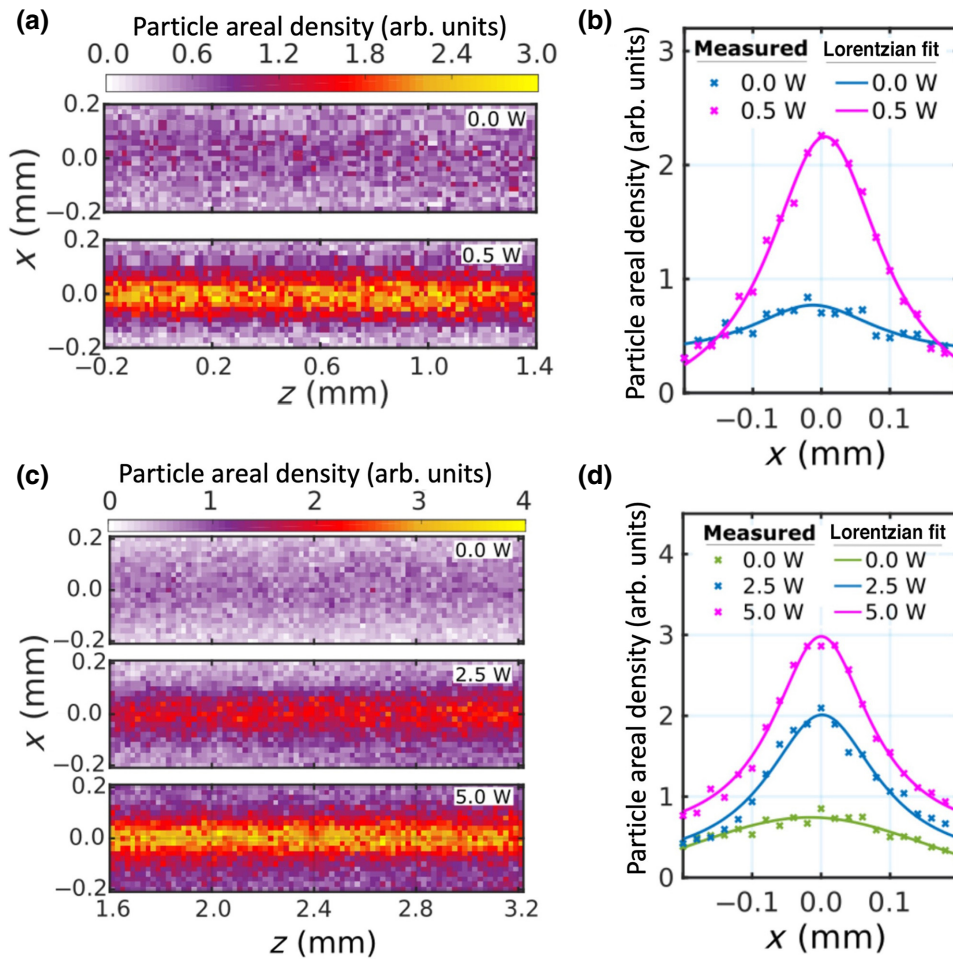


FIG. 4. The focusing of granulovirus particles at 0.4-mbar chamber pressure and 2- $\mu\text{m}$ -diameter polystyrene particles at 0.5-mbar chamber pressure. (a) Granulovirus particle areal-density maps with the laser off (top) and in the presence of a 0.5-W optical funnel (bottom). (b) The 2- $\mu\text{m}$ -diameter polystyrene particle areal-density maps with the laser off (top) and in the presence of 2.5-W (middle) and 5.0-W (bottom) optical-funnel illumination, respectively. The density maps in (a) and (b) are normalized to the peak density in the respective laser-off conditions. (c) The Lorentzian fit to the areal particle densities in (a), averaged over the  $z = [0.4, 0.6]$  mm region. (d) The Lorentzian fit to the areal particle density in (b), averaged over the  $z = [2.4, 2.6]$  mm region.

### B. Temperature gradient

Based on our measured velocities and accelerations, we can estimate the relative temperature gradient  $\Delta T/T$  across the particles. Since our measurements are made in the free molecular flow regime, the photophoretic force may be derived from gas-kinetic theory [25,41] and described by the equation

$$F^{\text{pp}} = \frac{\pi}{6} \alpha P r^2 \frac{\Delta T}{T}, \quad (1)$$

where  $r \approx 162$  nm is the effective radius of a granulovirus particle,  $P$  is the gas pressure, and  $\alpha \approx 1$  is the thermal-accommodation coefficient. The observed accelerations are dominated by three forces: the photophoretic force ( $\vec{F}^{\text{pp}}$ ), optical scattering and absorption forces ( $\vec{F}^{\text{opt}}$ ), and the gas drag force ( $\vec{F}^d$ ) [42]. As described in Sec. S-VII of

the Supplemental Material [32], we determine the velocity-dependent drag force empirically by fitting a line to the equation  $a = bv + c$  for our observed accelerations ( $a$ ) and velocities ( $v$ ) with the laser turned off. Under the conditions shown in Fig. 4, the values of the coefficients are  $b = -810 \text{ s}^{-1}$  and  $c = 43 \text{ m/s}^2$ . We expect the optical forces to be much lower than the maximum value of  $F_z^{\text{opt}} \approx \pi r^2 I / c \approx 8.3 \times 10^{-14} \text{ N}$ , which corresponds to full absorption at the peak intensity in the optical funnel ( $I = 3.0 \times 10^8 \text{ W/m}^2$ ). For the trajectory shown in Figs. 4(b)–4(e), upon subtracting the gas drag force, the combined photophoretic and optical force is  $6.2 \times 10^{-14} \text{ N}$ , which suggests that the photophoretic force is indeed dominant, as also suggested by the fact that such curved trajectories do not occur when the laser is turned off. The peak acceleration corresponds to a relative temperature gradient of  $\Delta T/T = 0.045$  and  $\Delta T \gtrsim 13 \text{ K}$  since  $T \gtrsim 298 \text{ K}$ .

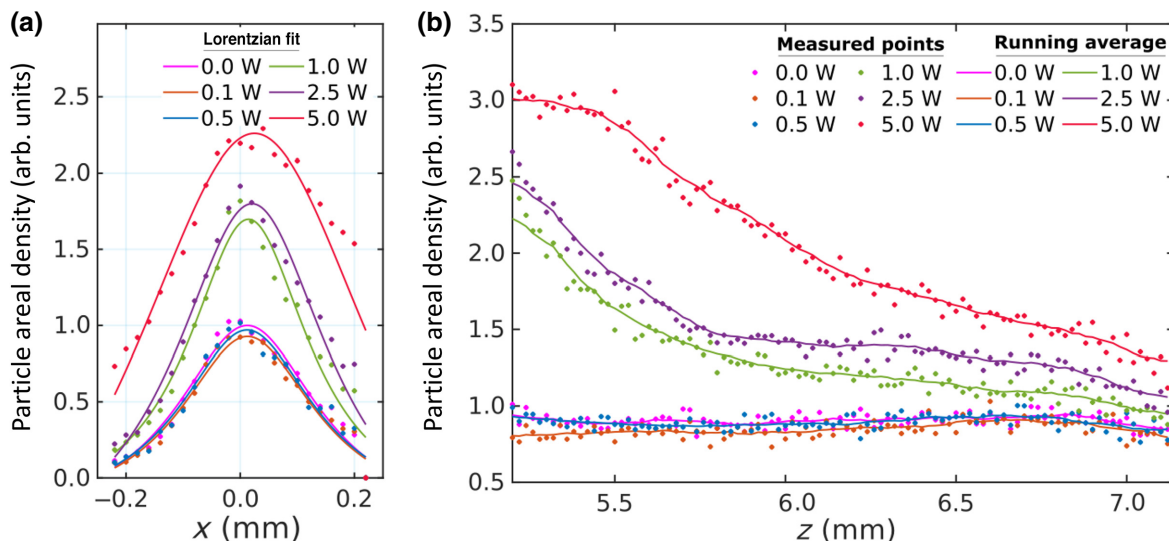


FIG. 5. The increase of the 2- $\mu\text{m}$ -diameter polystyrene particle number density at distances between 5.2 mm and 7.2 mm before the optical-funnel focus, for laser powers between 0 W and 5 W. (a) The radial cross section of the particle-beam density at  $z = 5.5$  mm from the optical-funnel focus. (b) The axial cross section along the axis of the particle beams. These number densities are normalized against the peak density with the laser off. The solid line represents the running average calculated over 12 successive points.

If we assume the thermal conductivity  $g$  of granulovirus to be approximately the same as most polymers and protein-based materials,  $g = 0.3 \text{ W}/(\text{mK})$ , then the intensity of heat transfer across the granulovirus at this temperature difference is of order  $I_{\text{heat}} \approx g\Delta T/r \approx 2.47 \times 10^7 \text{ W}/\text{m}^2$ , which is well below the typical threshold for radiation damage.

#### IV. CONCLUSIONS

In summary, our observations show clear evidence for the focusing of virus particles in a beam due to the photophoretic force in a low-pressure helium gas in the molecular-flow regime. We show that the density of the virus beam can be increased by a factor of 3 when turning on the optical funnel, which will proportionately reduce the measurement time and the amount of sample needed to perform x-ray diffraction measurements. The exact effects of the optical funnel are complicated by the nonlinear dynamics, which are sensitive to the initial particle-beam phase-space density, the surrounding gas pressure and gas velocity, the optical-funnel beam profile, and the precision of the alignment of the optical axis to the particle-beam axis. While it is clear that more detailed calculations and experiments are needed in order to fully understand and optimize an optical-funnel system, the results presented here clearly encourage further research. Based on acceleration measurements, we estimate the relative temperature gradient across the viruses, which is critical to understand as overheating of biological targets is a concern. However, future work that combines an optical funnel with cold particle beams would help avoid the

potential of overheating while simultaneously enhancing the magnitude of photophoretic force and greatly improving the aerodynamic focusing, especially when smaller particles are used [7].

#### ACKNOWLEDGMENTS

We acknowledge support by the Deutsches Elektronen-Synchrotron (DESY), a member of the Helmholtz Association (HGF), and the use of the Maxwell computational resources operated at DESY. This work has been supported by the Deutsche Forschungsgemeinschaft (DFG) through the Clusters of Excellence “Center for Ultrafast Imaging” (CUI, EXC 1074, Grant No. ID 194651731) and “Advanced Imaging of Matter” (AIM, EXC 2056, Grant No. ID 390715994), and by the European Research Council under the European Union’s Seventh Framework Programme (Grant No. FP7/2007-2013) through the Consolidator Grant COMOTION (Grant No. 614507) and by the Australian Research Council’s Discovery Projects funding scheme (Grant No. DP170100131). R.A.K. acknowledges support from the National Science Foundation (NSF) Biology with X-Ray Free Electron Lasers (BioXFEL) Science and Technology Center (STC) award under Grant No. 1231306 as well as NSF Biological Sciences (BIO) Division awards under Grants No. 1943448 and No. 1817862.

S.A., R.A.K., D.A.H., A.V.R., J.K., and H.N.C. conceived the idea and designed the experiment. S.A., D.A.H., N.R., R.A.K., and A.V.R. performed the measurements. S.A. and R.A.K. developed the particle data-analysis tool and analyzed the data. S.L.V. and A.V.R. performed the

optical beam modeling. S.A. wrote the initial version of the manuscript with inputs from R.A.K., S.L.V., and A.V.R. All authors contributed in scientific discussions and manuscript revisions.

The authors declare no competing interests.

- 
- [1] R. Neutze, R. Wouts, D. van der Spoel, E. Weckert, and J. Hajdu, Potential for biomolecular imaging with femtosecond X-ray pulses, *Nature* **406**, 752 (2000).
- [2] H. N. Chapman *et al.*, Femtosecond x-ray protein nanocrystallography, *Nature* **470**, 73 (2011).
- [3] H. N. Chapman, X-ray free-electron lasers for the structure and dynamics of macromolecules, *Annu. Rev. Biochem.* **88**, 35 (2019).
- [4] J. C. H. Spence, XFELs for structure and dynamics in biology, *IUCrJ* **4**, 322 (2017).
- [5] I. Schlichting, Serial femtosecond crystallography: The first five years, *IUCrJ* **2**, 246 (2015).
- [6] K. Ayyer *et al.*, 3D diffractive imaging of nanoparticle ensembles using an x-ray laser, *Optica* **8**, 15 (2021).
- [7] A. K. Samanta, M. Amin, A. D. Estillore, N. Roth, L. Worbs, D. A. Horke, and J. Küpper, Controlled beams of shock-frozen, isolated, biological and artificial nanoparticles, *Struct. Dyn.* **7**, 024304 (2020).
- [8] M. J. Bogan, W. H. Benner, S. Boutet, U. Rohner, M. Frank, A. Barty, M. M. Seibert, F. Maia, S. Marchesini, S. Bajt, B. Woods, V. Riot, S. P. Hau-Riege, M. Svenda, E. Marklund, E. Spiller, J. Hajdu, and H. N. Chapman, Single particle x-ray diffractive imaging, *Nano Lett.* **8**, 310 (2008).
- [9] J. Bielecki *et al.*, Electrospray sample injection for single-particle imaging with x-ray lasers, *Sci. Adv.* **5**, eaav8801 (2019).
- [10] N. Roth, S. Awel, D. A. Horke, and J. Küpper, Optimizing aerodynamic lenses for single-particle imaging, *J. Aerosol Sci.* **124**, 17 (2018).
- [11] S. Awel, R. A. Kirian, N. Eckerskorn, M. Wiedorn, D. A. Horke, A. V. Rode, J. Küpper, and H. N. Chapman, Visualizing aerosol-particle injection for diffractive-imaging experiments, *Opt. Express* **24**, 6507 (2016).
- [12] R. A. Kirian *et al.*, Simple convergent-nozzle aerosol injector for single-particle diffractive imaging with x-ray free-electron lasers, *Struct. Dyn.* **2**, 041717 (2015).
- [13] W. K. Murphy and G. W. Sears, Production of particulate beams, *J. Appl. Phys.* **35**, 1986 (1964).
- [14] P. Liu, P. J. Ziemann, D. B. Kittelson, and P. H. McMurry, Generating particle beams of controlled dimensions and divergence: I. Theory of particle motion in aerodynamic lenses and nozzle expansions, *Aerosol Sci. Techn.* **22**, 293 (1995).
- [15] P. Liu, P. J. Ziemann, D. B. Kittelson, and P. H. McMurry, Generating particle beams of controlled dimensions and divergence: II. Experimental evaluation of particle motion in aerodynamic lenses and nozzle expansions, *Aerosol Sci. Techn.* **22**, 314 (1995).
- [16] M. F. Hantke, J. Bielecki, O. Kulyk, D. Westphal, D. S. D. Larsson, M. Svenda, H. K. N. Reddy, R. A. Kirian, J. Andreasson, J. Hajdu, and F. R. N. C. Maia, Rayleigh-scattering microscopy for tracking and sizing nanoparticles in focused aerosol beams, *IUCrJ* **5**, 673 (2018).
- [17] L. Worbs, N. Roth, J. Lübke, A. D. Estillore, P. L. Xavier, A. K. Samanta, and J. Küpper, Optimizing the geometry of aerodynamic lens injectors for single-particle coherent diffractive imaging of gold nanoparticles, *J. Appl. Crystallogr.* **54**, 1730 (2021).
- [18] D. McGloin, D. R. Burnham, M. D. Summers, D. Rudd, N. Dewar, and S. Anand, Optical manipulation of airborne particles: Techniques and applications, *Faraday Discuss.* **137**, 335 (2008).
- [19] V. G. Shvedov, A. V. Rode, Y. V. Izdebskaya, A. S. Desyatnikov, W. Krolikowski, and Y. S. Kivshar, Giant Optical Manipulation, *Phys. Rev. Lett.* **105**, 118103 (2010).
- [20] D. R. Burnham and D. McGloin, Modeling of optical traps for aerosols, *J. Opt. Soc. Am. B* **28**, 2856 (2011).
- [21] V. G. Shvedov, A. S. Desyatnikov, A. V. Rode, W. Krolikowski, and Y. S. Kivshar, Optical guiding of absorbing nanoclusters in air, *Opt. Express* **17**, 5743 (2009).
- [22] D. E. Smalley, E. Nygaard, K. Squire, J. V. Wagoner, J. Rasmussen, S. Gneiting, K. Qaderi, J. Goodsell, W. Rogers, M. Lindsey, K. Costner, A. Monk, M. Pearson, B. Haymore, and J. Peatross, A photophoretic-trap volumetric display, *Nature* **553**, 486 (2018).
- [23] N. Eckerskorn, L. Li, R. A. Kirian, J. Küpper, D. P. DePonte, W. Krolikowski, W. M. Lee, H. N. Chapman, and A. V. Rode, Hollow Bessel-like beam as an optical guide for a stream of microscopic particles, *Opt. Express* **21**, 30492 (2013).
- [24] N. Eckerskorn, R. Bowman, R. A. Kirian, S. Awel, M. Wiedorn, J. Küpper, M. J. Padgett, H. N. Chapman, and A. V. Rode, Evaluation of Optically Induced Forces Imposed in an Optical Funnel on a Stream of Particles in Air and in Vacuum, *Phys. Rev. Appl.* **4**, 064001 (2015).
- [25] H. Rohatschek, Semi-empirical model of photophoretic forces for the entire range of pressures, *J. Aerosol Sci.* **26**, 717 (1995).
- [26] W. Zhu, N. Eckerskorn, A. Upadhyaya, L. Li, A. V. Rode, and W. M. Lee, Dynamic axial control over optically levitating particles in air with an electrically-tunable variable-focus lens, *Biomed. Opt. Express* **7**, 2902 (2016).
- [27] R. W. Bowman and M. J. Padgett, Optical trapping and binding, *Rep. Prog. Phys.* **76**, 026401 (2013).
- [28] J. H. McLeod, The axicon: A new type of optical element, *J. Opt. Soc. Am.* **44**, 592 (1954).
- [29] B. E. Saleh and M. C. Teich, *Fundamentals of Photonics* (Wiley-Interscience, Hoboken, New Jersey, 2007).
- [30] O. Brzobohatý, T. Čížmár, and P. Zemánek, High quality quasi-Bessel beam generated by round-tip axicon, *Opt. Express* **16**, 12688 (2008).
- [31] V. Jarutis, R. Paškauskas, and A. Stabinis, Focusing of Laguerre-Gaussian beams by axicon, *Opt. Commun.* **184**, 105 (2000).
- [32] See the Supplemental Material at <http://link.aps.org/supplemental/10.1103/PhysRevApplied.17.044044> for Modelling and formation of optical funnel (S-I, S-II); Sample preparation (S-III); Aerosol injection (S-IV); Particle imaging (S-V); Data analysis (S-VI); Estimation of forces and temperature gradients (S-VII); Positioning of the optical funnel

- in the camera FOV (S-VIII); and Experimental parameters (S-IX).
- [33] S. Lavin-Varela, M. Ploschner, and A. Rode, in *Optical Trapping and Optical Micromanipulation XVI*, edited by K. Dholakia and G. C. Spalding, International Society for Optics and Photonics (SPIE, 2019), Vol. 11083, p. 244.
- [34] C. Gati *et al.*, Atomic structure of granulin determined from native nanocrystalline granulovirus using an x-ray free-electron laser, *Proc. Natl. Acad. Sci. U.S.A.* **114**, 2247 (2017).
- [35] D. P. DePonte, U. Weierstall, K. Schmidt, J. Warner, D. Starodub, J. C. H. Spence, and R. B. Doak, Gas dynamic virtual nozzle for generation of microscopic droplet streams, *J. Phys. D* **41**, 195505 (2008).
- [36] K. R. Beyerlein, L. Adriano, M. Heymann, R. Kirian, J. Knoska, F. Wilde, H. N. Chapman, and S. Bajt, Ceramic micro-injection molded nozzles for serial femtosecond crystallography sample delivery, *Rev. Sci. Instrum.* **86**, 125104 (2015).
- [37] D. Oberthür *et al.*, Double-flow focused liquid injector for efficient serial femtosecond crystallography, *Sci. Rep.* **7**, 44628 (2017).
- [38] S. Awel *et al.*, Femtosecond X-ray diffraction from an aerosolized beam of protein nanocrystals, *J. Appl. Cryst.* **51**, 133 (2018).
- [39] M. Ester, H.-P. Kriegel, J. Sander, and X. Xu *et al.*, in *KDD-96: Proceedings of the Second International Conference on Knowledge Discovery and Data Mining* (1996), Vol. 96, p. 226.
- [40] M. L. Quillin and B. W. Matthews, Accurate calculation of the density of proteins, *Acta Cryst. D* **56**, 791 (2000).
- [41] H. Horvath, Photophoresis—a forgotten force ??, *KONA Powder and Particle Journal* **31**, 181 (2014).
- [42] D. K. Hutchins, M. H. Harper, and R. L. Felder, Slip correction measurements for solid spherical particles by modulated dynamic light scattering, *Aerosol Sci. Techn.* **22**, 202 (1995).